Supporting Information

Ferroelectricity and Piezoelectric Energy Harvesting of an $A_3M_2X_9$-type 0D Bromobismuthate Hybrid with Bulky Organic Quaternary Amine

Namonarayan Meena,[a,†] Supriya Sahoo,[a,†] Nilotpal Deka,[a] Vinayak B. Gadagin,[a] Jan K. Zaręba,[b,*] Ramamoorthy Boomishankar[a,*]

[a]Department of Chemistry and Centre for Energy Science, Indian Institute of Science Education and Research, Pune, Dr. Homi Bhabha Road, Pune – 411008, India

Email: boomi@iiserpune.ac.in

[b]Institute of Advanced Materials, Wrocław University of Science and Technology, 50-370 Wrocław, Poland

Email: jan.zareba@pwr.edu.pl

[†]*N.M. and S.S. contributed equally to this paper*

Table of contents

EXPERIMENTAL SECTION

General Remarks

4-Bromo-N,N-dimethylaniline was purchased from Merck, 4-methyl benzyl bromide was procured from Lobachemie, India and bismuth(II) oxide and hydrobromic acid were acquired from Avra Chemicals, India and directly employed without further purification. Thermogravimetric analyses were performed on the PerkinElmer STA-6000 analyzer, with a heating rate of 10°C/min, and the differential scanning calorimetry (DSC) measurements using a TA Q20 differential scanning calorimeter, with heating and cooling rates of 10°C/min. Both these measurements were performed under a dry nitrogen atmosphere. Melting points without correction were recorded on a Buchi M-560 melting point apparatus. The FT-IR spectra were obtained using the Bruker (Invenio R), covering the range of 400-4000 cm^{-1}. Powder X-ray diffraction (PXRD) data, in the 2θ range of 5 to 50º, were collected using the Bruker-D8 Advance X-ray diffractometer. The field-emission scanning electron microscopy (FE-SEM) images of all composite films (with different weight percentages of **[BPMBDMA]·[Bi_2Br_9]** were recorded using the Zeiss ultra plus FE-SEM instrument with a minimum spatial resolution of 1 µm.

Synthesis of [(*p*-BrPh)(*p*-MeBn)NMe_2]$_3$·[Bi_2Br_9]:

4-Methyl benzyl bromide (555.18 mg, 3 mmol) and 4-Bromo-N,N-dimethylaniline (600.24 mg, 3 mmol) was stirred in 5 ml of Acetonitrile. To this stirred solution added in a dropwise manner to a solution of Bi_2O_3 (465.96 mg, 1 mmol) in concentrated HBr (9 N, 4 mL) [Scheme S1]. The resulting solution was stirred for 30 minutes and the obtained yellow precipitate was collected by filtration. Yellow crystals of **[BPMBDMA]·[Bi_2Br_9]** suitable for single crystal X-ray diffraction analysis were obtained from its methanol solution after 7-8 days. Yield: 85%. FT-IR data in KBr pellet (cm^{-1}): 2923, 1700, 1621, 1455, and 1111. Anal. calcd. for **[BPMBDMA]·[Bi_2Br_9]**: Cal. C 27.31; H 2.54; N 2.08. Found: C 27.41; H 2.50; N 2.10.

Single Crystal X-ray Diffraction Analysis:

The single-crystal X-ray diffraction data for compound **[BPMBDMA]·[Bi_2Br_9]** were collected on a Bruker Smart Apex Duo diffractometer with Mo Kα radiation (λ = 0.71073 Å). The crystal structures were solved through the direct method and refined using full-matrix least-squares against F^2, employing the SHELXL-2014/7 program integrated into the Apex 3 software.[1] Anisotropic refinement was applied to all nonhydrogen atoms, while hydrogen atoms were constrained in geometric positions relative to their parent atoms.[2] Structural illustrations were generated using the DIAMOND-3.1 software.

Hirshfeld Surface Analysis:

The Crystal Explorer 3.1 program was employed to perform Hirshfeld surface analysis on **[BPMBDMA]·[Bi_2Br_9]**. For Hirshfeld analysis, the single-crystal X-ray crystallographic information file (CIF) was utilized and the diverse interactions present in **[BPMBDMA]·[Bi_2Br_9]** were visualized. The resulting 3D color mapping images illustrate the surface characteristics of the compound **[BPMBDMA]·[Bi_2Br_9]**; red: intense interactions, blue: medium interactions, and white: weak interactions. A 2D fingerprint plot, essentially a histogram, was generated by compiling distances between atoms closest to the interior (d_i) and exterior (d_e) of the Hirshfeld surface. The plot featured various contours represented by blue and grey colors, offering valuable insights into the various molecular interactions present in the molecule.

Nonlinear Optical Measurements:

The Kurtz-Perry powder tests were conducted using a Coherent Astrella Ti: Sapphire regenerative amplifier (RA) to generate femtosecond laser pulses with a repetition rate of 1 kHz. These laser pulses were directed through a wavelength-tuneable Topaz Prime Vis-NIR optical parametric amplifier (OPA) to achieve the desired wavelength of 1300 nm. The laser beams, with a fluence of 0.20 mJ cm^{-2} at 1300 nm, were unfocused. The SHG relative efficiency of **[BPMBDMA]·[Bi_2Br_9]** was determined through the Kurtz-Perry powder method, utilizing potassium dihydrogen phosphate (KDP) as the SHG reference. Microcrystals of **[BPMBDMA]·[Bi_2Br_9]** and KDP were independently ground and sieved using an Aldrich mini-sieve set to obtain a microcrystal size fraction of 250−177 µm. The laser beam was directed at the samples at an angle of 45°, and the diffused SHG spectra were recorded by an Ocean Optics Flame T spectrograph after suppressing the scattered pumping radiation with a 750 nm short-pass dielectric filter.

Ferroelectric, Dielectric and Piezoelectric Measurements:

To investigate the ferroelectric properties of **[BPMBDMA]·[Bi_2Br_9]**, *P-E* hysteresis loop measurements were conducted on a thin film sample of approximately 1.3 µm thickness drop-casted on an Indium tin oxide (ITO)-coated glass surface, and Gallium Indium eutectic was used to the make top contact. These measurements were performed using the aixACCT TF-2000E model hysteresis loop analyzer. The experiments were conducted by

applying the dynamic leakage current compensation (DLCC) mode to reduce the contributions from non-hysteretic components of the loop.

The dielectric permittivity of **[BPMBDMA]·[Bi_2Br_9]** was measured on its powder-pressed pellet sample. The measurements were conducted using the Solartron Analytical 1260 model Impedance Analyzer combined with a Dielectric Interface model 1296A. The sample was placed in a Janis 129610A cryostat sample holder, and the temperature was controlled using a Lakeshore 336 model temperature controller.

Piezoresponse Force Microscopy (PFM) Characterizations:

The PFM measurements were conducted using the Asylum Research MFP-3D atomic force microscopy (AFM) system for a drop-casted thin film of **[BPMBDMA]·[Bi_2Br_9]** on ITO-coated glass surface. A contact mode AFM experiment was carried out, utilizing RMN-12PT300B cantilever probes with a spring constant of 1.12 N m^{-1} and a tip diameter of less than 8 nm to measure the piezoresponse of the crystal films. Vertical-PFM experiments were employed to acquire PFM data, with the bottom electrode being grounded, while an AC voltage was applied to the conductive AFM tip. PFM images were collected at the resonance frequency of 300 +/- 20 kHz with an applied bias of 60 and 80 V. The measurements were performed using the dual AC resonance tracking (DART) mode of the PFM. The switching ability of the domains of the single crystal located on the thin film was recorded by the application of external DC bias of ±90 V using the PFM tip in contact mode.

General Procedure for the Preparation of Polymer Composite Films and Devices:

To fabricate composite films of **[BPMBDMA]·[Bi_2Br_9]**, different proportions (5, 10, 15, and 20 wt%) of ferroelectric crystallites were dispersed in a nonpiezoelectric, biodegradable polylactic acid polymer (PLA) dissolved in chloroform ($CHCl_3$). The solutions underwent mechanical stirring at 50 ˚C for 15 minutes, followed by vortex mixing for 15 minutes to ensure homogeneity. Subsequently, these solutions were poured onto a glass slide and left undisturbed to air-dry at room temperature for 8 hours. The resulting composite films were carefully peeled off from the glass slide, and copper conductive adhesive tapes were affixed to both sides to establish electrical contacts. To complete the architecture, the devices were covered with Kapton tapes. A pristine PLA polymer film encapsulated with Kapton tape was also prepared and subjected to similar experimental conditions for comparative analysis.

Piezoelectric Energy Harvesting and Storage Measurements:

An in-house-designed periodic impact set-up was employed to conduct mechanical energy harvesting experiments, applying an impact force of 21 N. The Tektronix 2024 Mixed Signal Oscilloscope, featuring an input impedance of 1 MΩ, was utilized for measuring output voltages and currents. The test devices, with a thickness of approximately 0.5 mm and an active area of 300 mm^2, were subjected to examination. To assess the energy storage capabilities of the devices during impact measurements, a 10 µF capacitor was connected to the device using a full-wave bridge four-diode circuit.

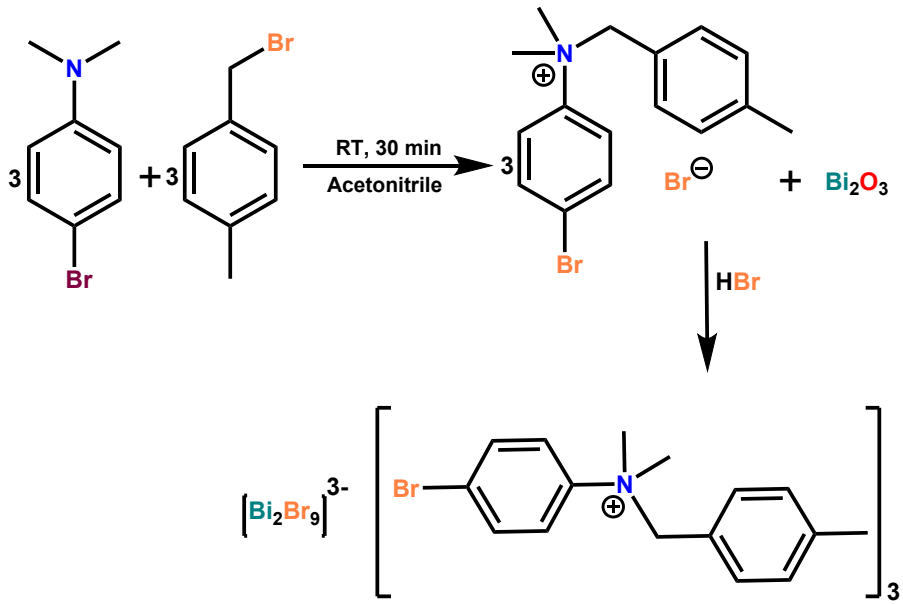

Scheme S1. Schematic showing the synthesis of **[BPMBDMA]·[Bi_2Br_9]**.

Table S1. X-ray Crystallographic data for **[BPMBDMA]·[Bi_2Br_9]**.

Crystallographic details	**[(*p*-BrPh)(*p*-MeBn)NMe_2]$_3$·[Bi_2Br_9].MeOH (150 K)**	**[(*p*-BrPh)(*p*-MeBn)NMe_2]$_3$·[Bi_2Br_9].MeOH (298 K)**
Chemical formula	$C_{49}H_{57}Bi_2Br_{12}N_3O$	$C_{49}H_{57}Bi_2Br_{12}N_3O$
Formula weight (g/mol)	2052.81	2052.81
Temperature	150.15(2)	298.15(2)
Crystal system	Orthorhombic	Orthorhombic
Space group	*Pca*2_1	*Pca*2_1
a (Å); α (°)	28.426(12); 90	28.880(7); 90
b (Å); β (°)	11.954(5); 90	12.092(3); 90
c (Å); γ (°)	18.491(8); 90	18.540(4); 90
V (Å^3); Z	6283(4); 4	6475(3); 4
ρ (calc.) g cm^{-3}	2.200	2.135
μ (Mo K_α) mm^{-1}	13.260	12.868
$2\theta_{max}$ (°)	50.372	49.998
R(int)	0.2335	0.1648
Completeness to θ	99.5	100.0
Data / param.	11223/622	11398/548
GOF	1.093	1.193
R_1 [F>4σ(F)]	0.0500	0.0596
wR_2 (all data)	0.1301	0.1178
max. peak/hole (e.Å^{-3})	2.29/-2.19	1.47/-1.33

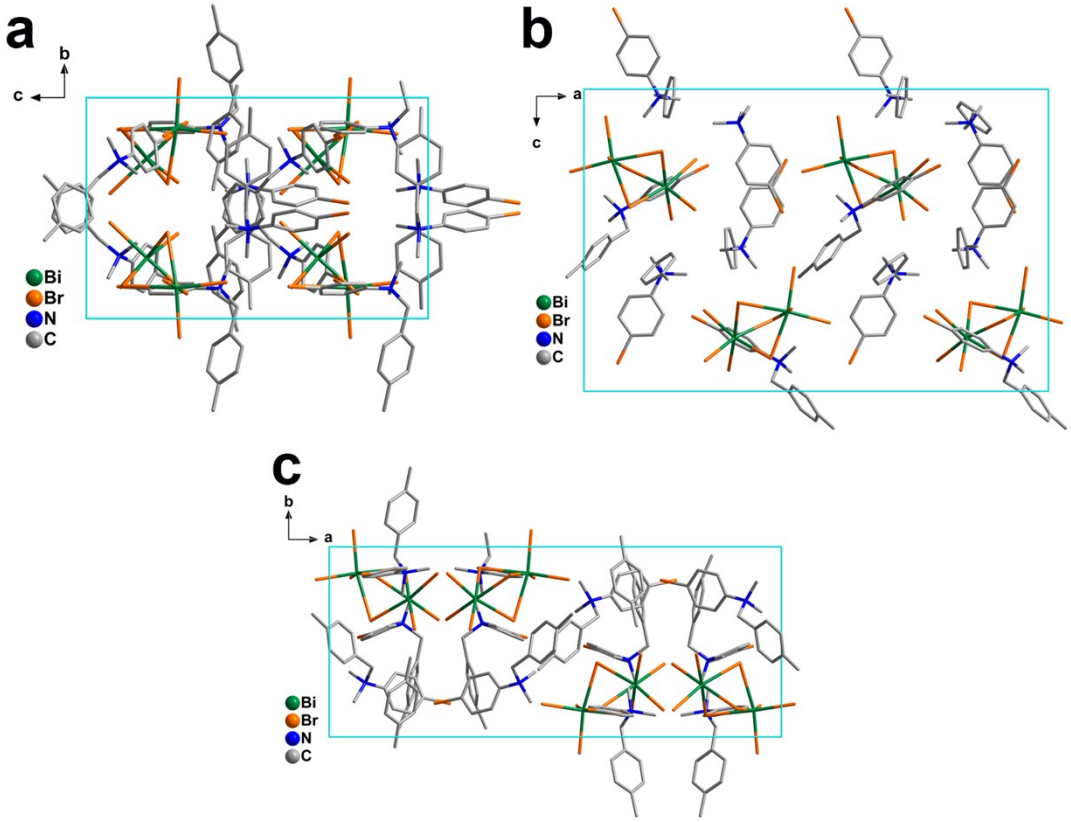

Figure S1. The packing diagram of **[BPMBDMA]·[Bi_2Br_9]** along (a) *a*-axis, (b) *b*-axis (c) *c*-axis at 150 K. Disordered solvent molecule has been omitted for clarity.

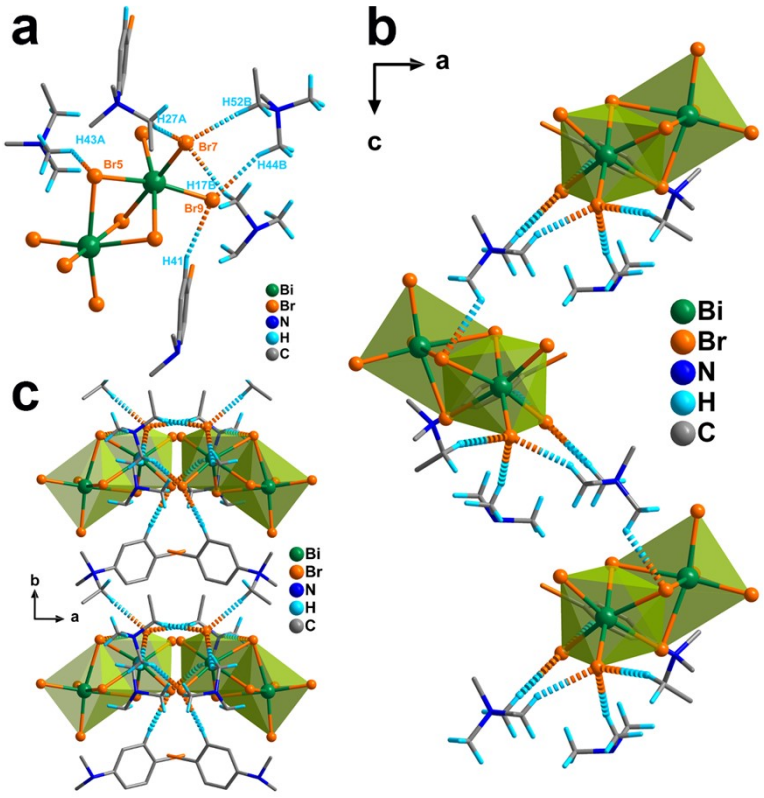

Figure S2. The C-H···Br hydrogen bonding interactions in **[BPMBDMA]·[Bi_2Br_9]** at 150 K.

Table S2. Hydrogen bonding parameters for **[BPMBDMA]·[Bi_2Br_9]** at 150 K.

D-H···A	d(H···A) Å	d(D-A) Å	<(DHA)
C(52)-H(52B)···Br(7)	2.7364(108)	3.6244(283)	156.139(1623)
C(27)-H(27A)···Br(7)	2.8613(121)	3.6388(250)	164.186(1434)
C(17)-H(17B)···Br(7)	2.8589(26)	3.5932(304)	132.473(1755)
C(41)-H(41A)···Br(9)	2.8173(26)	3.7209(244)	158.500(1454)
C(44)-H(44B)···Br(9)	2.8398(26)	3.7726(317)	158.960(1806)
C(43)-H(43A)···Br(5)	2.8577(27)	3.3929(227)	115.181(1311)

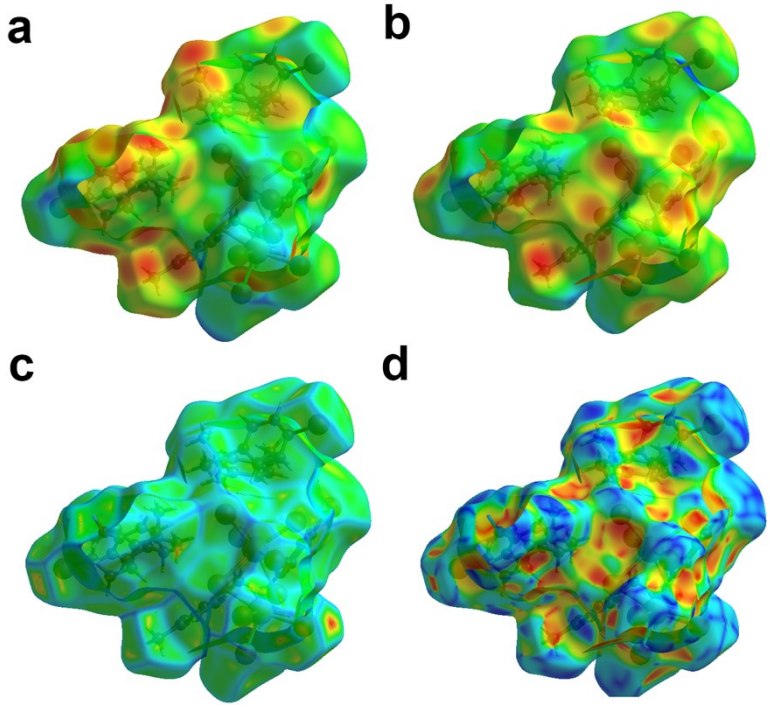

Figure S3. The 3D color mapping surfaces derived from the Hirshfeld surface analysis of **[BPMBDMA]·[Bi_2Br_9]**(150 K) showing (a) d_i, (b) d_e, (c) curvedness, and (d) shape index.

Table S3. Hirshfeld surface analysis of **[BPMBDMA]·[Bi_2Br_9]** at 150 K.

Temperature	Surface Property	Range (Minimum/Maximum)	Globularity and Asphericity	Surface Volume and Area
120 K	d_i	0.987/3.120	0.626 and 0.036	1506.17 Å^3 and 1015.85 Å^2
	d_e	0.809/3.195		
	d_{norm}	-0.539/1.650		
	Shape index	-0.999/0.999		
	Curvedness	-4.059/0.831		

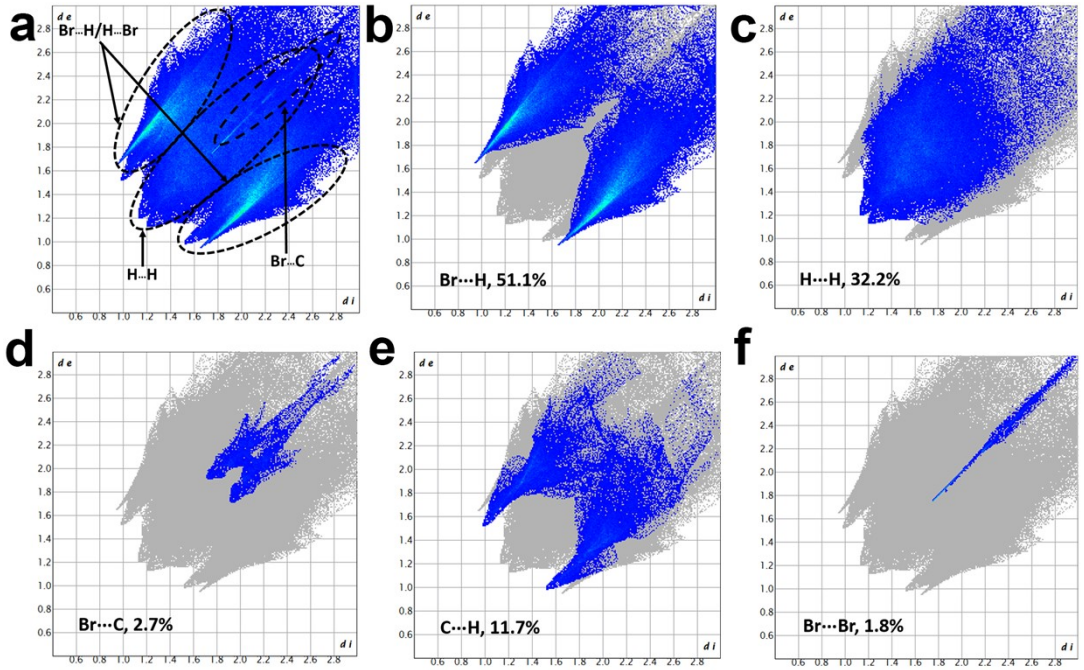

Figure S4. 2D fingerprint (d_e vs. d_i) plots of **[BPMBDMA]·[Bi_2Br_9]** (150 K) showing the percentages of (a) all interactions, , (b) Br···H/H···Br, (c) H···H (d) Br···C/C···Br, (e) C···H, and (f) Br···Br interactions.

Table S4. Percentage interactions present in **[BPMBDMA]·[Bi_2Br_9]** at 150 K.

Atom	Bi	Br	O	N	C	H	Total
Bi	-	-	-	-	-	-	0.0
Br	-	1.1	0.5	-	4.6	25.6	32.0
C	-	2.6	-	-	0.9	6.1	9.7
H	-	18.2	1.6	-	8.5	30.1	58.3
N	-	-	-	-	-	-	0.0
O	-	-	-	-	-	-	0.0
Total	0.0	21.9	2.1	0.0	14.1	61.9	

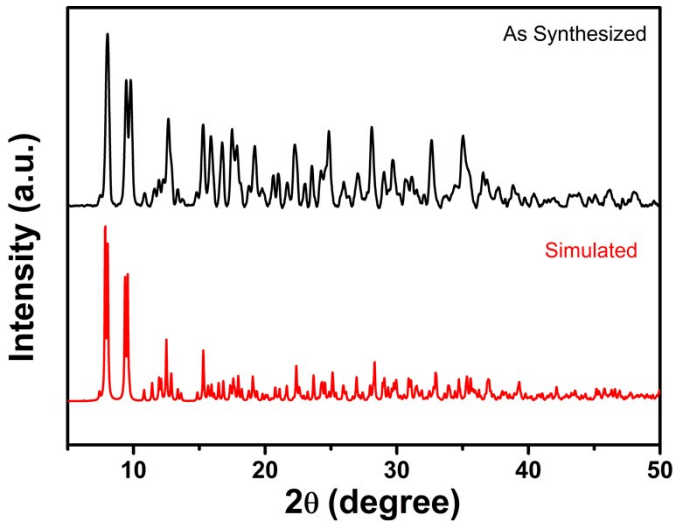

Figure S5. The room temperature PXRD profile of **[BPMBDMA]·[Bi_2Br_9]** along with its simulated profile from the 298 K SCXRD data.

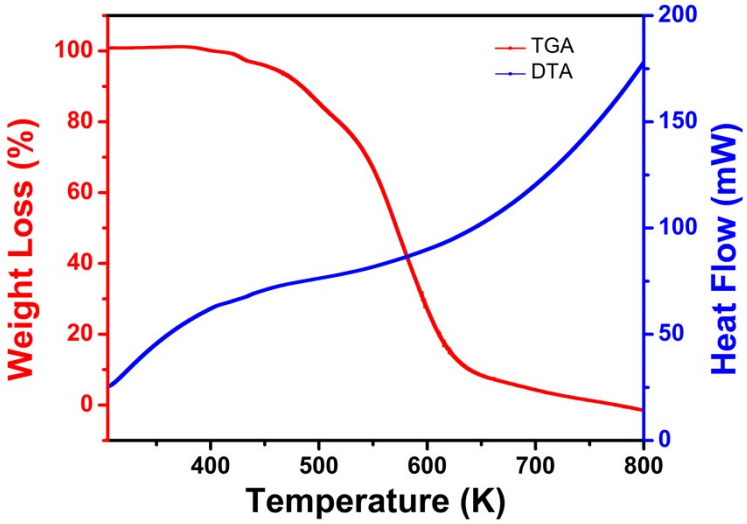

Figure S6. The thermogravimetric and differential thermal analysis profiles of **[BPMBDMA]·[Bi_2Br_9]**.

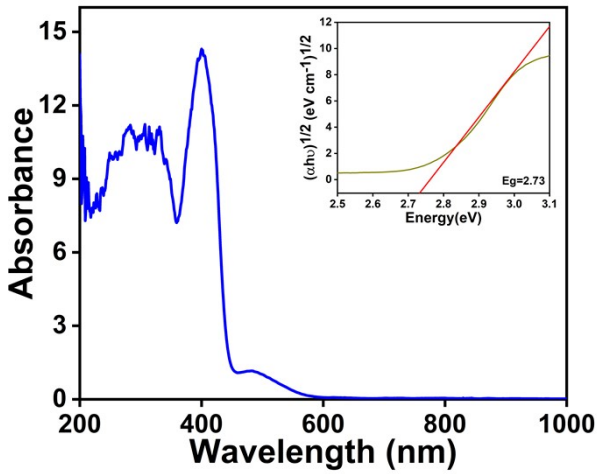

Figure S7. The UV-Vis diffuse reflectance spectrum of **[BPMBDMA]·[Bi_2Br_9]**. The corresponding Tauc plot is displayed in the inset.

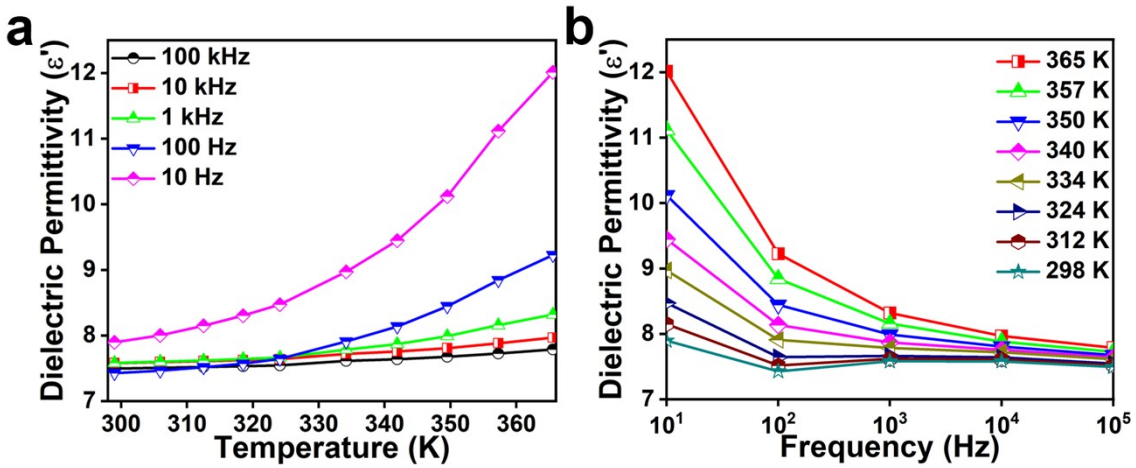

Figure S8. The (a) temperature-dependent (b) frequency-dependent dielectric permittivity plots of **[BPMBDMA]·[Bi_2Br_9]**.

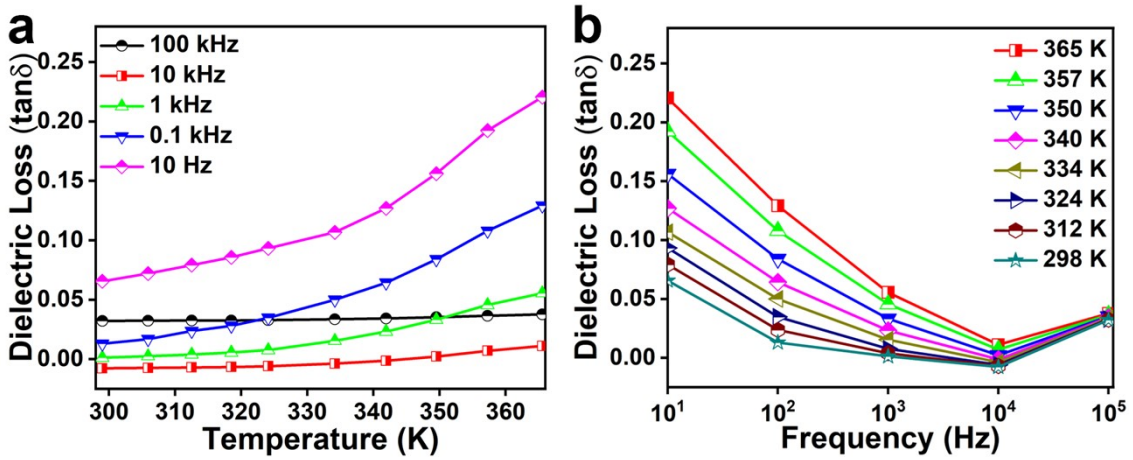

Figure S9. The (a) temperature-dependent (b) frequency-dependent dielectric loss profiles of **[BPMBDMA]·[Bi_2Br_9].**

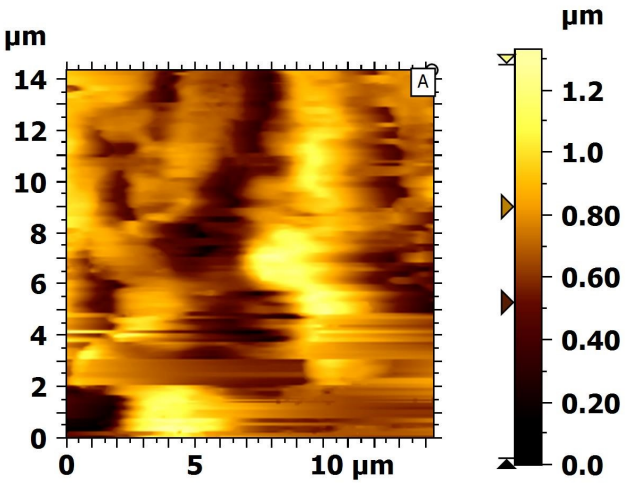

Figure S10. The atomic force microscopy (AFM) image of drop casted thin film sample of **[BPMBDMA]·[Bi_2Br_9]** on ITO-coated glass substrate.

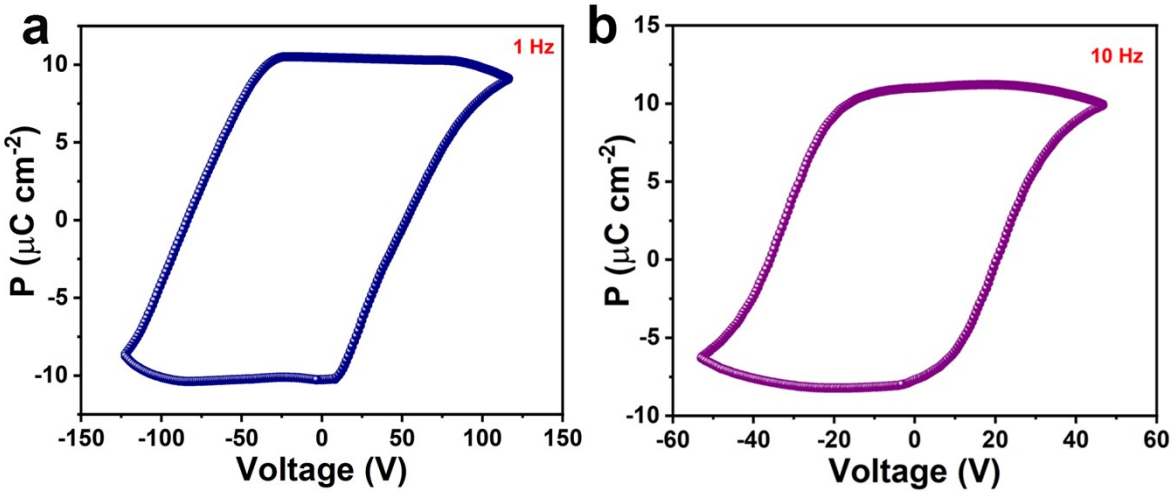

Figure S11. P-E loop measurements at different voltage and frequency at 298 K (a) 120 V and 1 Hz (b) 55 V and 10 Hz.

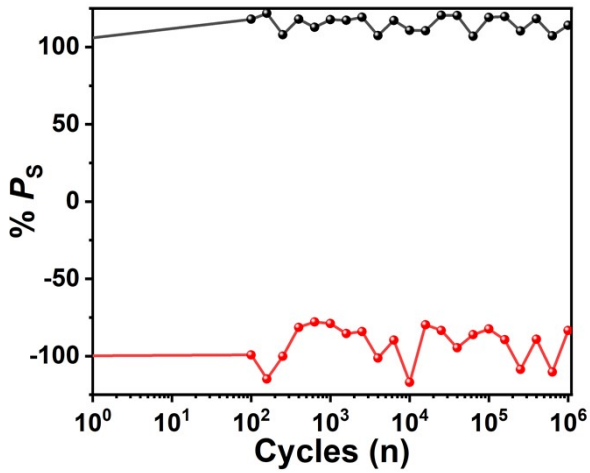

Figure S12. The fatigue test showing the retention of polarization of **[BPMBDMA]·[Bi_2Br_9]** up to 10^6 cycles at 298 K.

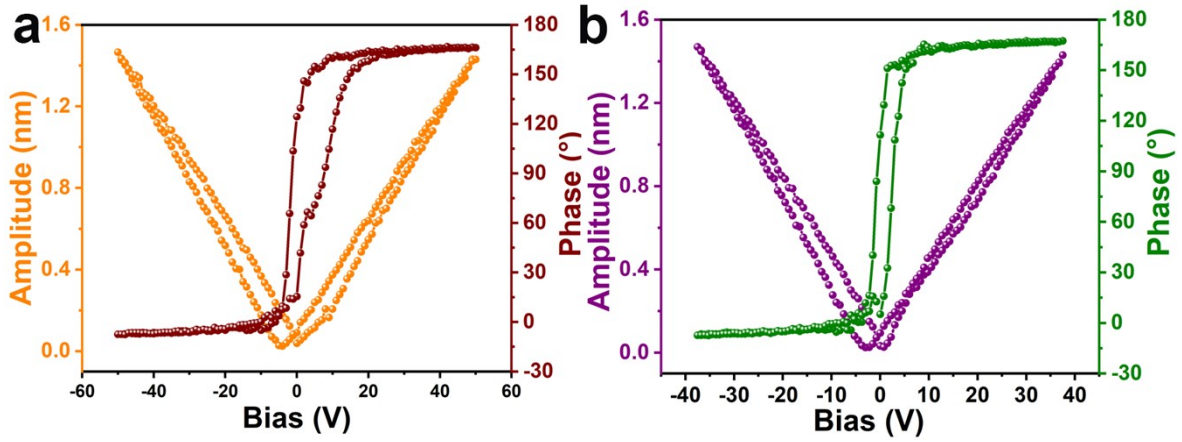

Figure S13. PFM 'butterfly loop' and phase hysteresis loop at different voltages showing consistency across the voltage range.

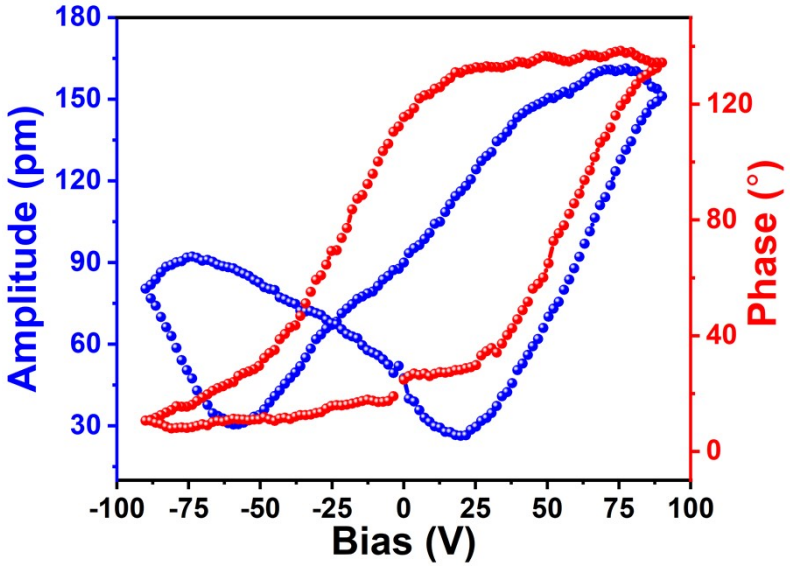

Figure S14. The off-state PFM amplitude-bias butterfly and phase-bias hysteresis loops for **[BPMBDMA]·[Bi_2Br_9]**.

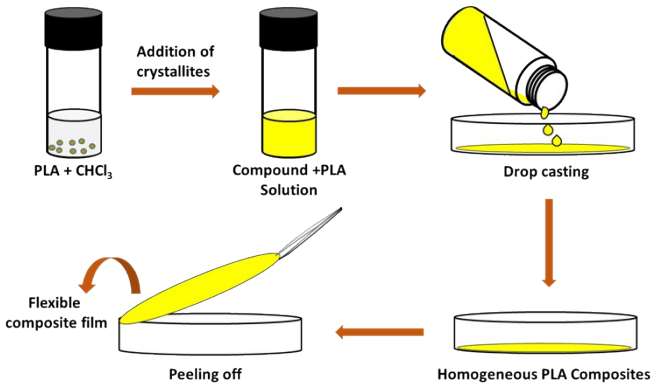

Figure S15. Schematic for the preparation of **[BPMBDMA]·[Bi_2Br_9]**-PLA composite films.

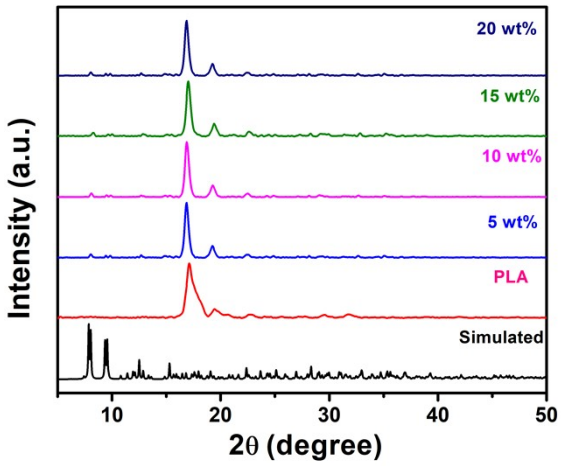

Figure S16. The PXRD profiles of **[BPMBDMA]·[Bi_2Br_9]**-PLA composites and their comparison with neat PLA and simulated PXRD pattern of **[BPMBDMA]·[Bi_2Br_9]**.

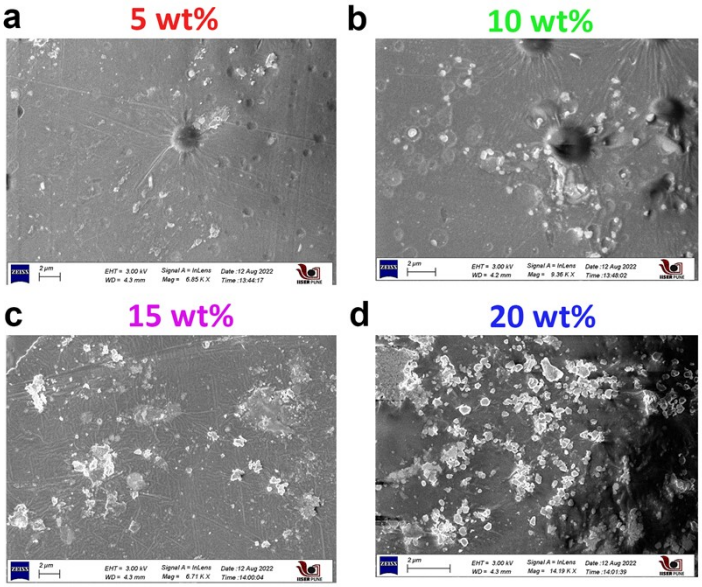

Figure S17. The FE-SEM images of 5, 10, 15, and 20 wt% **[BPMBDMA]·[Bi_2Br_9]**-PLA composite films.

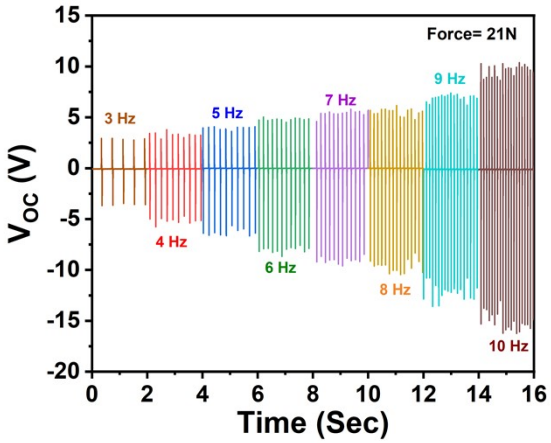

Figure S18. Frequency-dependent trend in V_{OC} values of the 10 wt% **[BPMBDMA]·[Bi_2Br_9]-**PLA device.

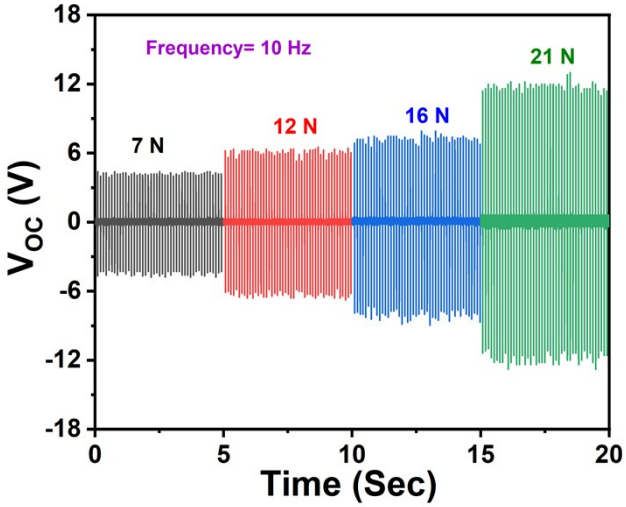

Figure S19. Force-dependent V_{OC} measurements for the 10 wt% **[BPMBDMA]·[Bi_2Br_9]-**PLA device.

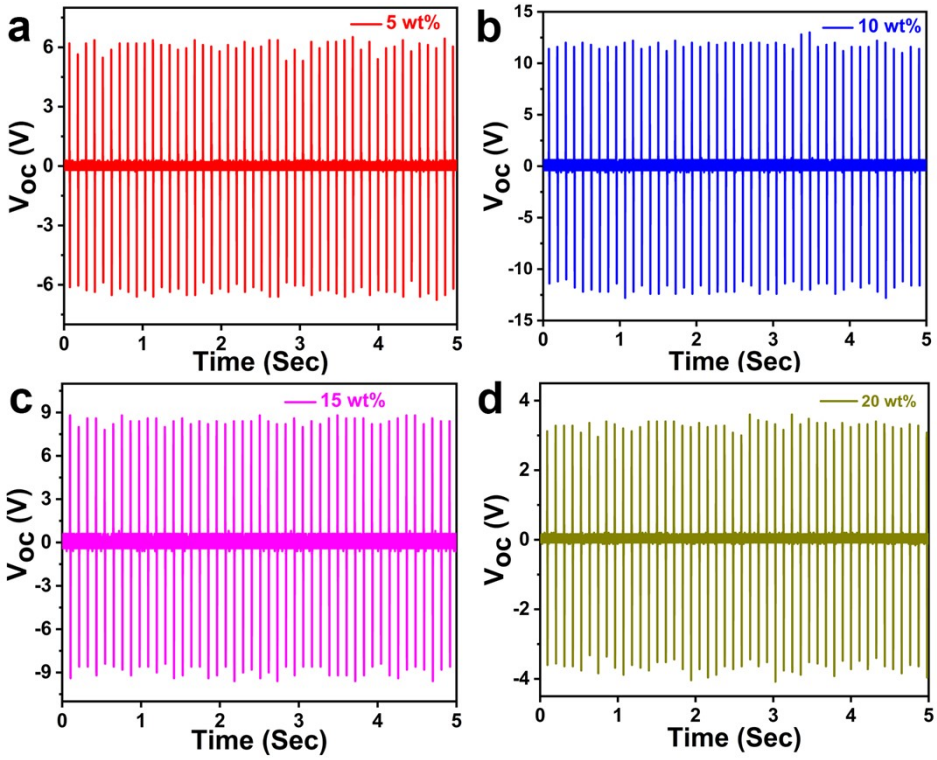

Figure S20. The open-circuit peak-to-peak voltage (V_{PP}) profiles of **[BPMBDMA]·[Bi_2Br_9]**-PLA composite devices.

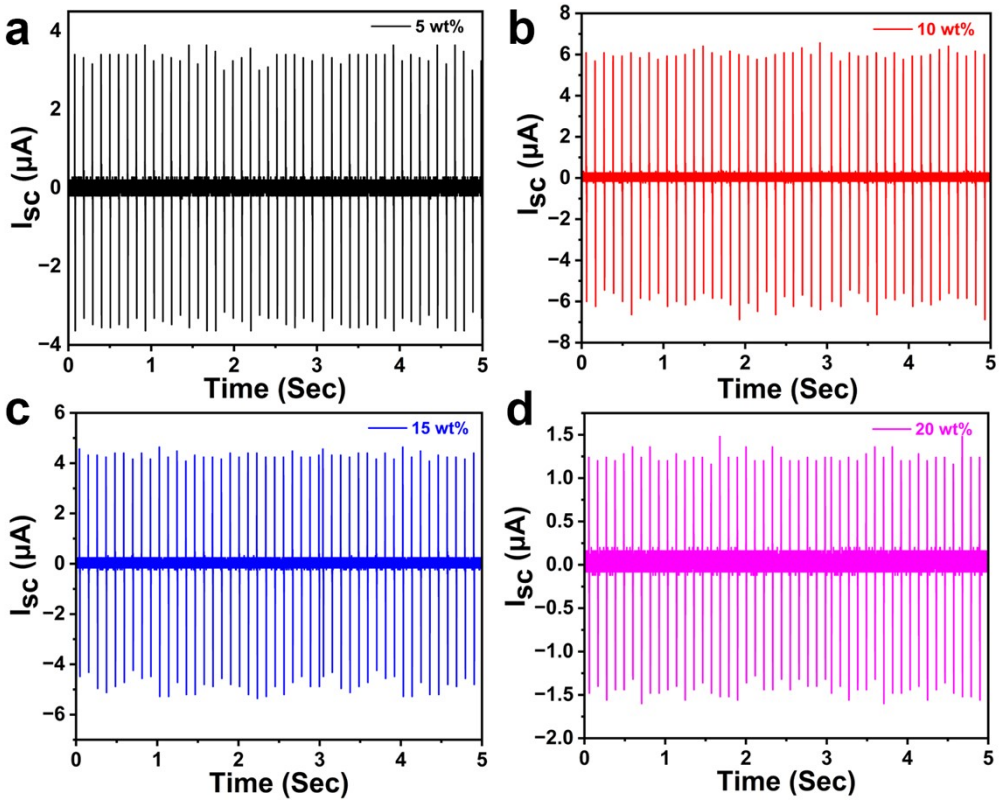

Figure S21. The output peak-to-peak current (I_{PP}) profile as calculated from the voltage drop obtained by attaching a 1 MΩ resistor across the circuit for the **[BPMBDMA]·[Bi_2Br_9]**-PLA composite devices.

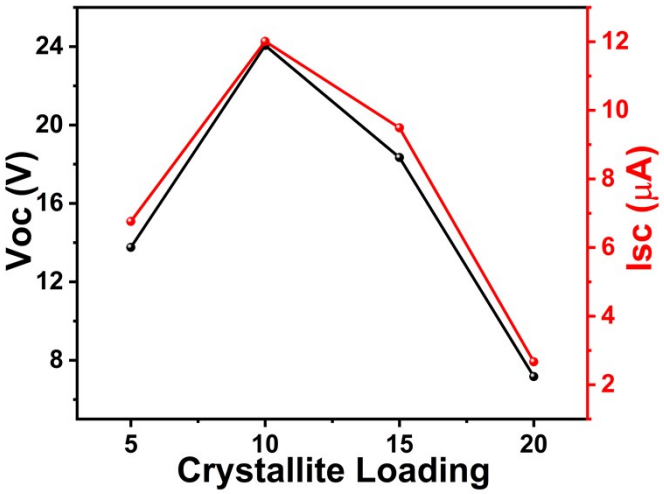

Figure S22. Comparative diagram showing the observed trends in V_{PP} and I_{PP} values of **[BPMBDMA]·[Bi_2Br_9]**-PLA composite devices.

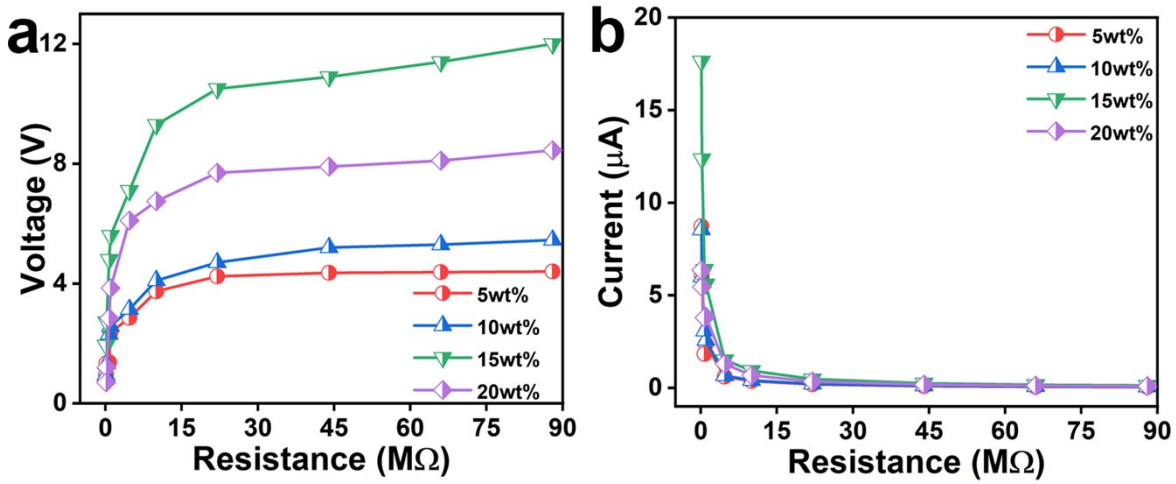

Figure S23. The comparative peak (a) voltage drop and (b) current data for all the **[BPMBDMA]·[Bi_2Br_9]**-PLA composite devices under various load resistances.

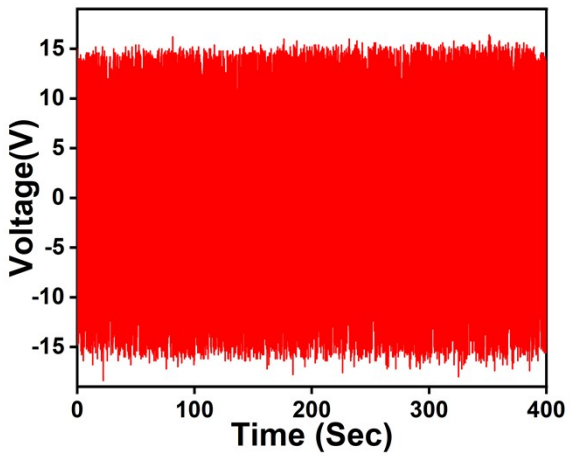

Figure S24. The cyclic stability test of 10 wt% **[BPMBDMA]·[Bi_2Br_9]**-PLA showing the retention of V_{PP} up to 4000 cycles.

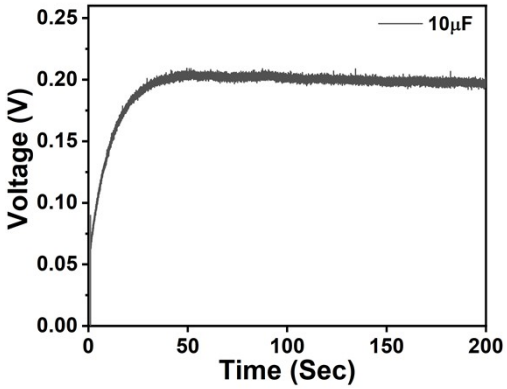

Figure S25. Voltage accumulated in a 10 μF capacitor by utilizing the 10 wt% **[BPMBDMA]·[Bi_2Br_9]**-PLA composite device.

Table S5. Comparison of output device performances of known hybrid composite energy harvesters.

Hybrid Composite Devices	Output Voltages	Power/Power density	Active area	References
$MAPbI_3$-PVDF	9.43	-	1 x 1 cm^2	[3]
$MAPbBr_3$-PVDF	5	0.28 μW cm^{-2}	2.4 x 1.5 cm^2	[4]
$MAPbI_3$-PDMS	1.0	-	1 x 1 cm^2	[5]
$FAPbBr_3$–PDMS	4	-	1 x 1 cm^2	[6]
$CsPbBr_3$/PVDF	10.3	3.31 μW	1 x 1 cm^2	[7]
PVDF–PLLA–SnO_2 NF–$MAPbI_3$	4.82	-	0.25 x 0.25 cm^2	[8]
SnO_2 NF–$MAPbI_3$	1.02	-	0.25 x 0.25 cm^2	[8]
$[BnNMe_3]_2CdBr_4$/PDMS	52.9	13.8 μW cm^{-2}	3 x 3 cm^2	[9]
$[BnNMe_2{}^nPr]_2CdBr_4$/PDMS	63.8	37.1 μW cm^{-2}	3 x 3 cm^2	[9]
$(TMFM)FeBr_4$	2.2	-	-	[10]
$[Ph_2(^iPrNH)_2P]_3[Fe(CN)_6]$-TPU	13.57	6.03 μW cm^{-2}	1.3 x 3 cm^2	[11]
$[Me(Ph)_3P]_3[Bi_2Br_9]$-PDMS	22.9	7 μW cm^{-2}	1.5x1.5 cm^2	[12]
$[Ph_3MeP]_4[Ni(NCS)_6]$/TPU	19.29	2.51 mW cm^{-3}	1.3 x 3 cm^2	[13]
$[Ph_3PMe]_4[CuCl_4]$-TPU	25	14.1 μW cm^{-2}	1.2 x 3 cm^2	[14]
$\{[^sCH(MePh)(Me)NH_3][BiBr_5]\}_n$-PLA	10.4	5.26 μW Cm^{-2}	1.2 x 3 cm^2	[15]
$[BP_{Br}DMA]_2\cdot[BiBr_5]$	26.2	15.47 μW Cm^{-2}	1 x 3 cm^2	[16]
[BPMBDMA]·[Bi_2Br_9]	24.6	13.65 μW Cm^{-2}	1 x 3 cm^2	This Work

Note: $MAPbI_3$ = methylammonium lead iodide; PVDF = polyvinylidene difluoride; PDMS = polydimethysiloxane; $FAPbBr_3$ = formamidinium lead bromide; PLLA = poly(L-lactic acid); SnO_2 = tin oxide; NF = nanofiber; $[BnNMe_3]_2CdBr_4$ = N,N,N-trimethyl-1-phenylmethanaminium cadmium(II) bromide; $[BnNMe_2{}^nPr]_2CdBr_4$ = N-benzyl-N,N-dimethylpropan-1-aminium cadmium(II) bromide; $(TMFM)FeBr_4$ = trimethylfluoromethylammonium iron(III)bromide; TPU

= thermoplastic polyurethane; Ph = Phenyl, Bn = Benzyl, ^{i}Pr = isopropyl, Me = Methyl; $BP_{Br}DMA$= *N*-benzyl-4-bromo-*N*,*N*-dimethylbenzenaminium.

References:

1. G. M. Sheldrick, *Acta Crystallogr. A: Found. Adv.*, 2008, **64**, 112-122.
2. A. L. Spek, *Acta Crystallogr. D Biol. Crystallogr.*, 2009, **65**, 148-155.
3. V. Jella, S. Ippili, J.-H. Eom, J. Choi and S.-G. Yoon, *Nano Energy*, 2018, **53**, 46-56.
4. A. Sultana, M. M. Alam, P. Sadhukhan, U. K. Ghorai, S. Das, T. R. Middya and D. Mandal, *Nano Energy*, 2018, **49**, 380-392.
5. Y.-J. Kim, T.-V. Dang, H.-J. Choi, B.-J. Park, J.-H. Eom, H.-A. Song, D. Seol, Y. Kim, S.-H. Shin and J. Nah, *J. Mater. Chem. A*, 2016, **4**, 756-763.
6. R. Ding, H. Liu, X. Zhang, J. Xiao, R. Kishor, H. Sun, B. Zhu, G. Chen, F. Gao and X. Feng, *Adv. Funct. Mater.*, 2016, **26**, 7708-7716.
7. Y. Li, M.-h. Xu, Y.-s. Xia, J.-m. Wu, X.-k. Sun, S. Wang, G.-h. Hu and C.-x. Xiong, *Chem. Eng. J.*, 2020, **388**, 124205.
8. R. Tusiime, F. Zabihi, M. Tebyetekerwa, Y. M. Yousry, Y. Wu, M. Eslamian, S. Yang, S. Ramakrishna, M. Yu and H. Zhang, *J. Mater. Chem. C*, 2020, **8**, 2643-2658.
9. S. Deswal, S. K. Singh, P. Rambabu, P. Kulkarni, G. Vaitheeswaran, B. Praveenkumar, S. Ogale and R. Boomishankar, *Chem. Mater.*, 2019, **31**, 4545-4552.
10. Y. Zhang, X.-J. Song, Z.-X. Zhang, D.-W. Fu and R.-G. Xiong, *Matter*, 2020, **2**, 697-710.
11. T. Vijayakanth, S. Sahoo, P. Kothavade, V. Bhan Sharma, D. Kabra, J. K. Zaręba, K. Shanmuganathan and R. Boomishankar, *Angew. Chem. Intl. Ed.*, 2023, **62**, e202214984.
12. S. Deswal, R. Panday, D. R. Naphade, P. Dixit, B. Praveenkumar, J. K. Zaręba, T. D. Anthopoulos, S. Ogale and R. Boomishankar, *Chem. Eur. J.*, 2022, **28**, e202200751.
13. T. Vijayakanth, F. Ram, B. Praveenkumar, K. Shanmuganathan and R. Boomishankar, *Angew. Chem. Intl. Ed.*, 2020, **59**, 10368-10373.
14. S. Sahoo, T. Vijayakanth, P. Kothavade, P. Dixit, J. K. Zaręba, K. Shanmuganathan and R. Boomishankar, *ACS Mater. Au*, 2022, **2**, 124-131.
15. S. Sahoo, N. Deka and R. Boomishankar, *CrystEngComm*, 2022, **24**, 6172-6177.
16. N. Meena, S. Sahoo, N. Deka, J. K. Zaręba and R. Boomishankar, *Inorg. Chem.*, 2024, **63**, 9245-9251.